Supplement for

Comparing 3m resolution snow cover downscaled from MODIS, VIIRS, and HLS using commercial satellite imagery and terrain information

Justin M. Pflug[a,b], Kehan Yang[c,b], Nicoleta Cristea[d,e], Emma T. Boudreau[d], Carrie M. Vuyovich[b], Sujay V. Kumar[b]

[a]Earth System Science Interdisciplinary Center, University of Maryland, College Park, College Park, Maryland, USA
[b]Hydrological Sciences Laboratory, NASA Goddard Space Flight Center, Greenbelt, Maryland, USA
[c]Science Systems and Applications, Inc., Lanham, Maryland, USA
[d]Department of Civil and Environmental Engineering, University of Washington, Seattle, Washington, USA
[e]eScience Institute, University of Washington, Seattle, Washington, USA

Contents of this file: Figures S1 to S22, Table S1, and Table S2

Introduction

The information included here provides context and support for the results in the corresponding article text, but is not necessary for the understanding of the methods or results.

Table S1. Median *k* statistic and *k* standard deviation (parentheses) for each downscaling approach and sensor combination in every domain, and averaged across all domains (rightmost column). Dark green cells indicate the best downscaling approach for each column, and light green cells indicate the second-best downscaling approach.

Downscaling	Sensor	DAN	DPO	GIN	STR	551	737	869	All doms.
Terrain-based	MODIS	0.20 (0.08)	0.15 (0.13)	0.19 (0.14)	0.11 (0.07)	0.11 (0.10)	0.07 (0.08)	0.13 (0.10)	0.14 (0.11)
	VIIRS	0.17 (0.09)	0.42 (0.11)	0.20 (0.15)	0.34 (0.08)	0.12 (0.09)	0.22 (0.10)	0.16 (0.09)	0.23 (0.14)
	HLS	0.23 (0.18)	0.49 (0.15)	0.36 (0.25)	0.33 (0.19)	0.17 (0.13)	0.47 (0.22)	0.33 (0.19)	0.34 (0.22)
Probabilistic	MODIS	0.39 (0.12)	0.22 (0.19)	0.24 (0.15)	0.21 (0.12)	0.39 (0.23)	0.28 (0.15)	0.28 (0.18)	0.29 (0.18)
	VIIRS	0.41 (0.13)	0.52 (0.10)	0.28 (0.12)	0.53 (0.09)	0.34 (0.13)	0.38 (0.16)	0.34 (0.15)	0.40 (0.16)
	HLS	0.29 (0.18)	0.53 (0.15)	0.39 (0.25)	0.39 (0.21)	0.22 (0.13)	0.52 (0.23)	0.35 (0.20)	0.38 (0.22)
Random forest	MODIS	0.33 (0.17)	0.30 (0.23)	0.18 (0.15)	0.34 (0.14)	0.28 (0.20)	0.38 (0.14)	0.31 (0.18)	0.30 (0.19)
	VIIRS	0.30 (0.19)	0.42 (0.17)	0.21 (0.12)	0.52 (0.13)	0.35 (0.17)	0.34 (0.15)	0.35 (0.16)	0.35 (0.18)
	HLS	0.47 (0.21)	0.57 (0.13)	0.33 (0.18)	0.53 (0.21)	0.48 (0.14)	0.53 (0.19)	0.46 (0.12)	0.48 (0.19)

Table S2. Idealized model that represents the percentage of the signal that can come from outside the nominal MODIS cell based on the MODIS point spread function, off-nadir viewing angle, and terrain slope, assuming that the slope angle and off-nadir viewing angle are in the same direction.

Off-Nadir viewing angle (deg)	Slope angle (deg, assumed same direction as off-nadir)	Percentage of information from outside the nominal cell
0	0	41.9%
0	10	42.9%
0	20	44.2%
0	30	47.2%
15	0	45.7%
15	10	47.9%
15	20	51.6%
15	30	56.8%
30	0	57.1%
30	10	61.1%
30	20	66.1%
30	30	72.9%
45	0	73.8%
45	10	78.1%
45	20	83.8%
45	30	89.9%
55	0	84.9%
55	10	88.7%
55	20	93.1%
55	30	97.5%

Table S3. Accuracy of HLS fSCA estimates, relative to PS snow cover coarsened to the HLS grid. Results are presented for the fSCA derived using the NDSI to fSCA conversion (NDSI; Salomonson and Appel, 2006) and snow covered area and grain size approach (SCAG; Painter et al., 2009). Results are broken down by domain (rows), with the best-performing approach for each metric represented by the bolded value.

	fSCA temporal coefficient of correlation (r)		Mean fSCA bias		fSCA root-mean squared error		Snow frequency coefficient of determination	
	SCAG	NDSI	SCAG	NDSI	SCAG	NDSI	SCAG	NDSI
DAN	0.54	**0.97**	**0.06**	0.18	**0.17**	0.18	**0.87**	0.43
DPO	0.78	**0.99**	0.03	0.03	0.15	**0.04**	**0.70**	0.50
GIN	0.76	**0.93**	-0.17	**0.01**	0.24	**0.09**	**0.60**	0.26
STR	0.69	**0.98**	-0.12	**0.11**	0.22	**0.12**	**0.47**	0.42
551	0.73	**0.76**	**-0.15**	0.23	**0.16**	0.23	**0.61**	0.59
737	0.70	**0.98**	**-0.03**	0.08	0.12	**0.08**	0.36	**0.54**
869	0.97	0.97	**-0.03**	0.13	**0.07**	0.13	**0.78**	0.65

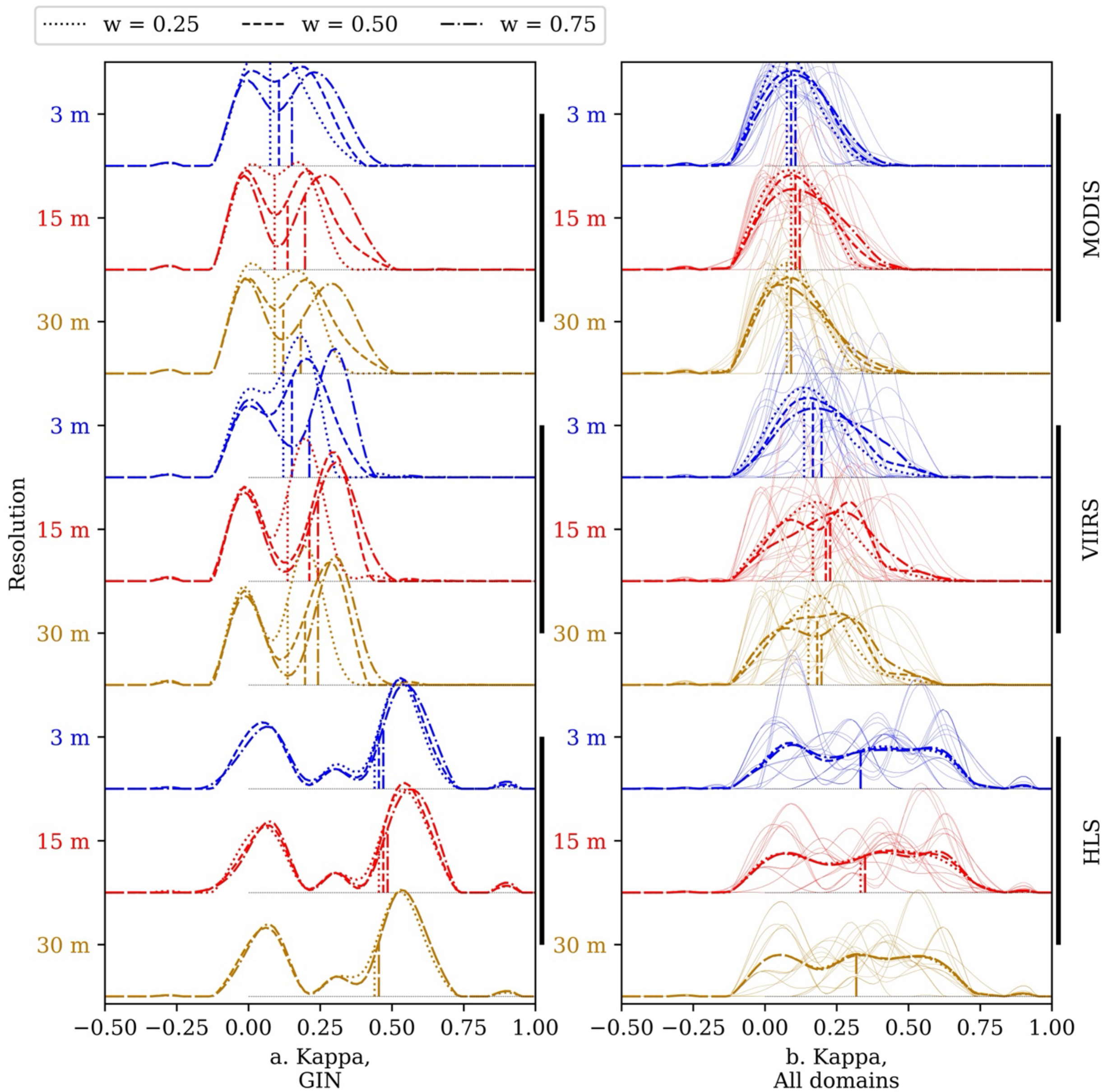

Figure S1. Distribution of *k*, relative to PS snow cover, including only dates when the domain-scale fSCA was between 0.15 and 0.85. Results include GIN (a, left) and all domains (b, right), and compare the performance of the terrain-based downscaling approach using three different fSCA datasets (right y-axis, black bars), SVI maps calculated at various resolutions (left y-axis and colors), and SVI maps using various weighting factors (line styles).

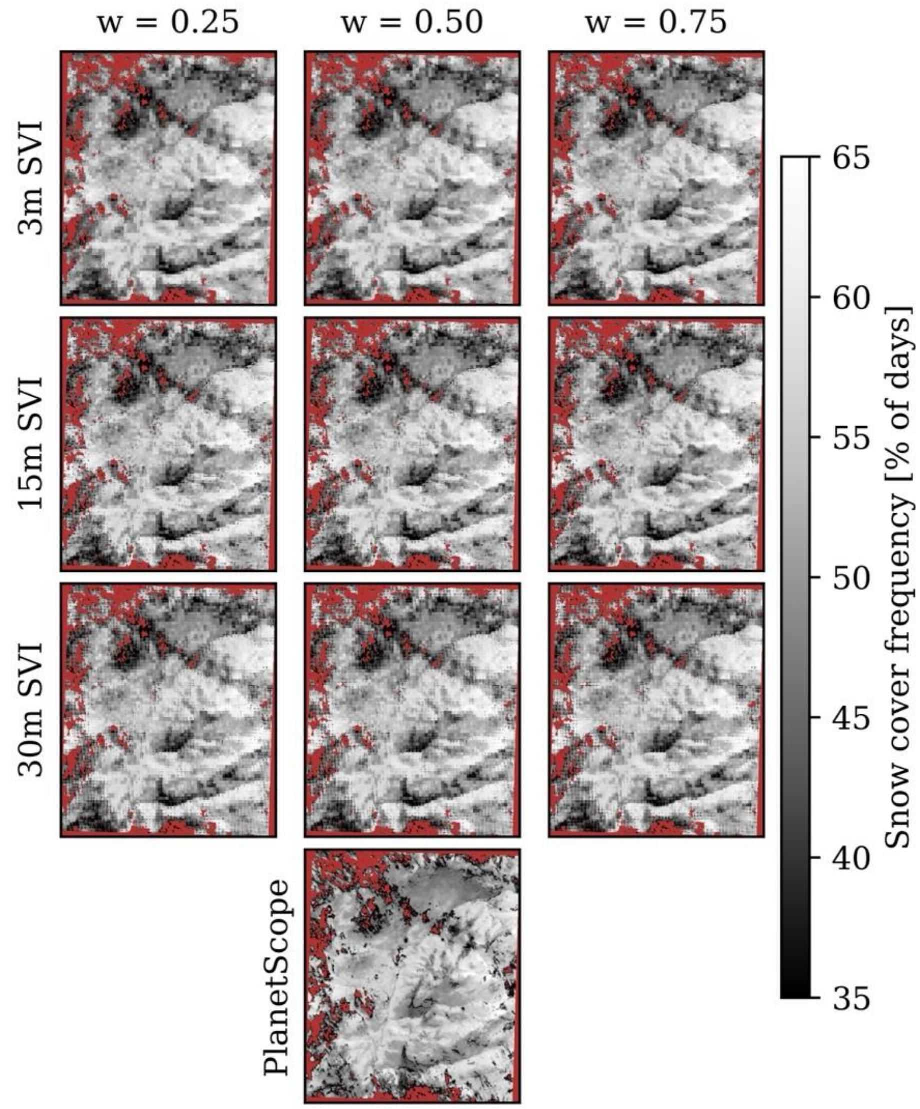

Figure S2. 3 m snow cover frequency on dates with PS snow cover observations (2019 – 2023) in GIN. Each estimate is downscaled using the terrain-based approach, fSCA from HLS, SVI maps at various resolutions (y-labels), and various weighting factors (top x-labels). Results are compared versus the 3 m pattern of snow cover frequency observed by PlanetScope (bottom subplot).

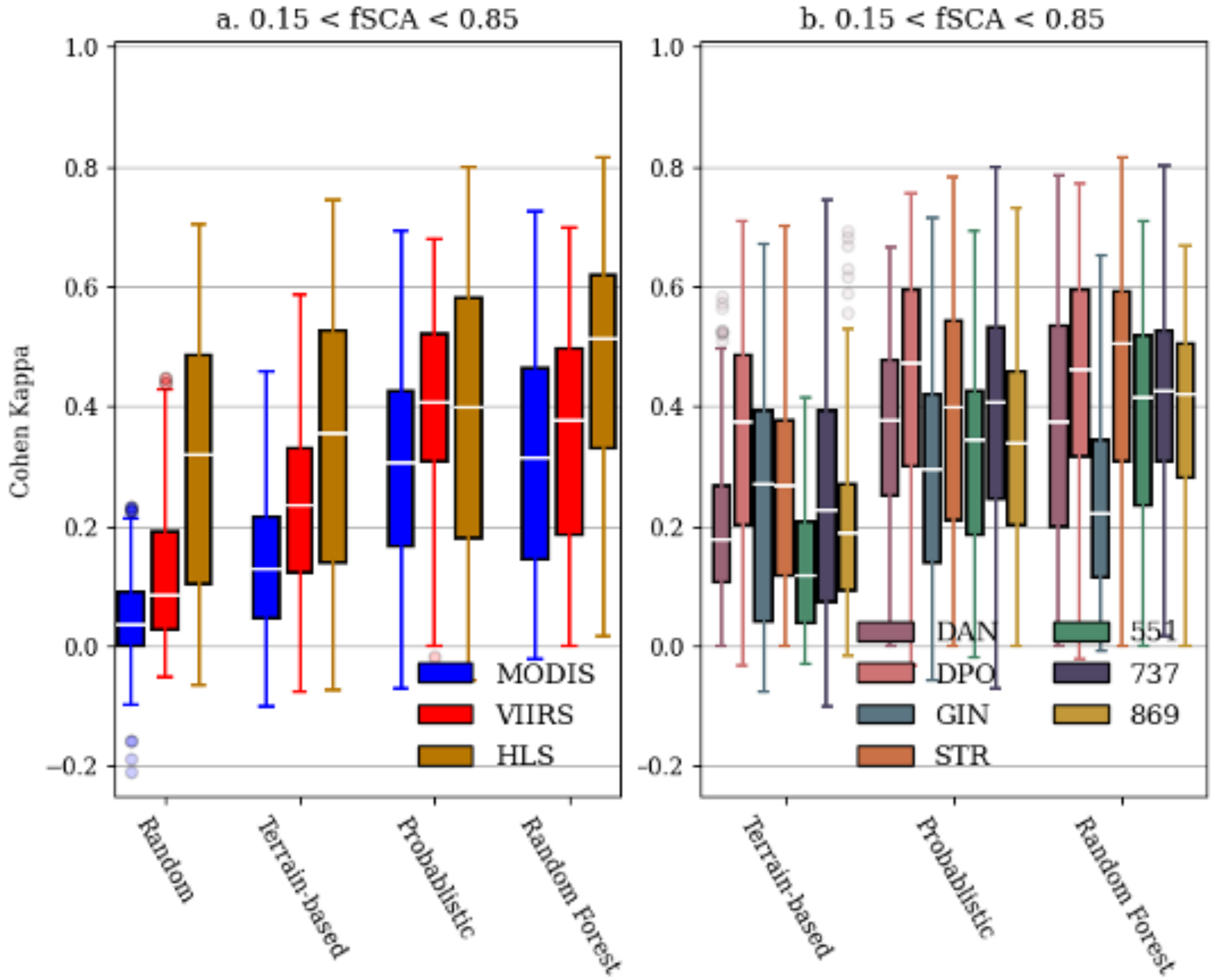

Figure S3. Distributions of *k*, relative to 3 m PS snow cover on dates with domain-scale fSCA between 0.15 and 0.85. Subplots show results stratified by the source of the fSCA estimate (a) and the domain (b).

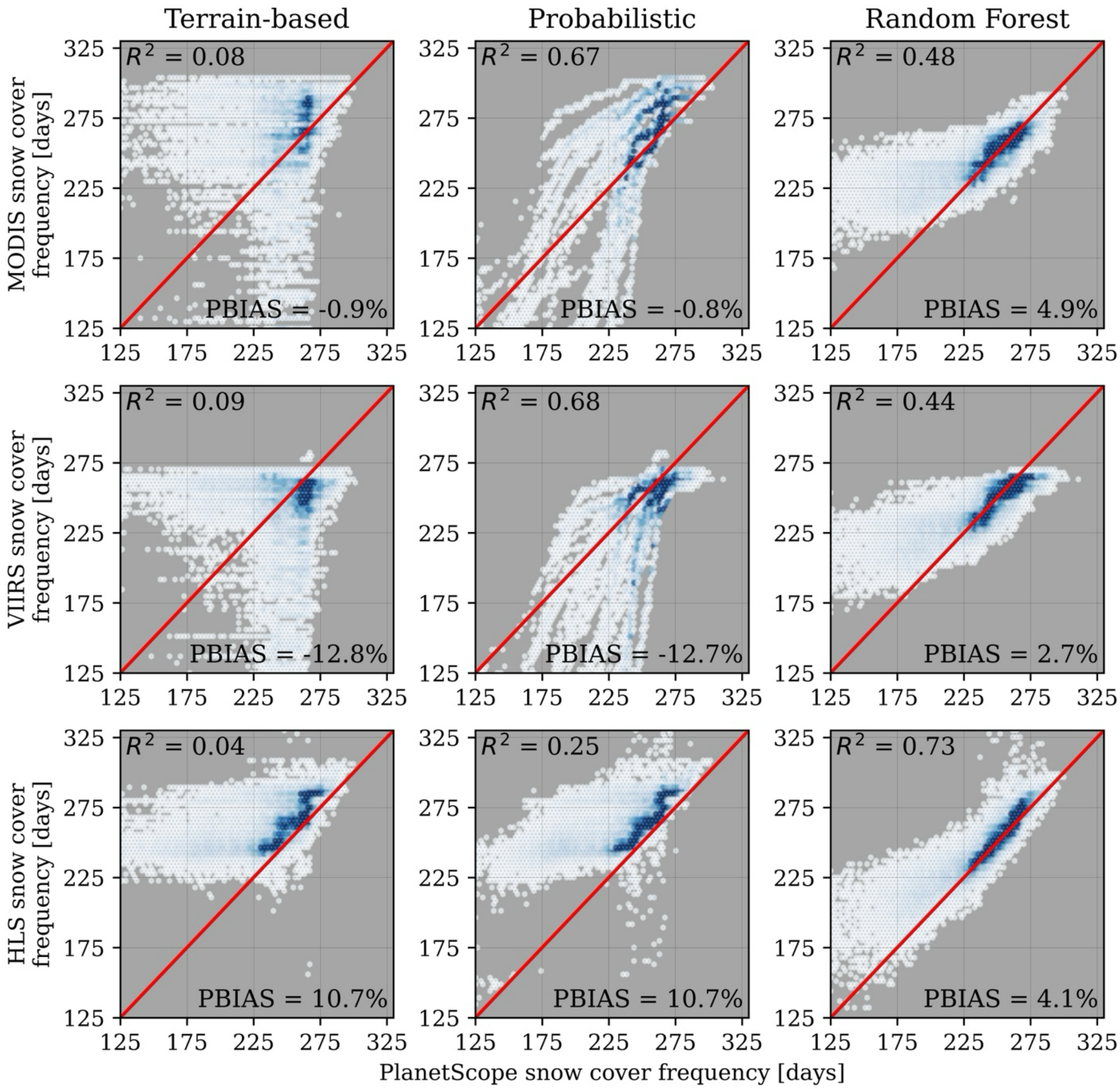

Figure S4. 3 m snow cover frequency estimated in the DAN domain from each sensor (rows) downscaled using the terrain-based, probabilistic, and random forest approaches (columns) compared to PS snow cover frequency (x-axes). Blue areas represent areas with higher point density.

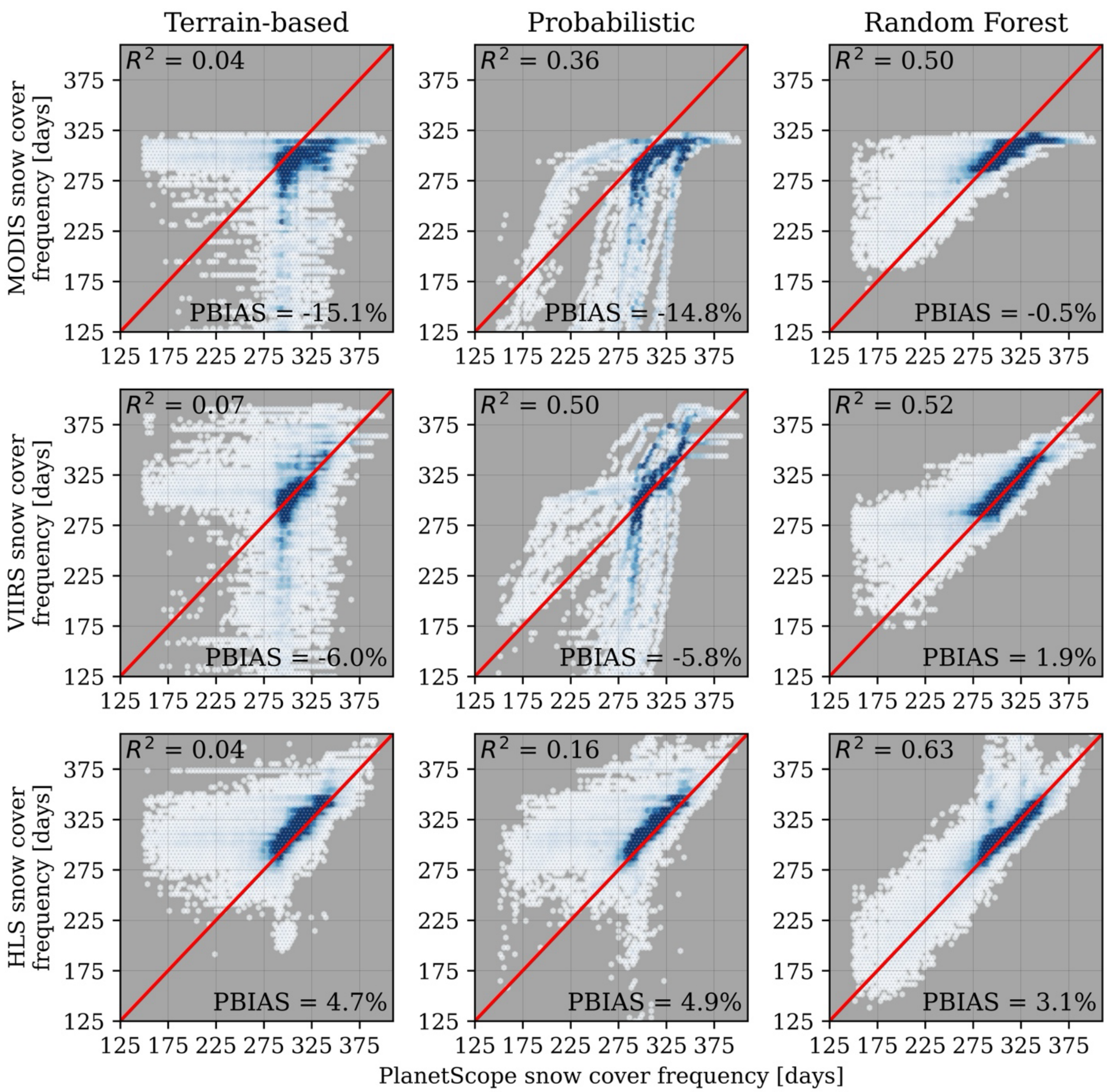

Figure S5. 3 m snow cover frequency estimated in the DPO domain from each sensor (rows) downscaled using the terrain-based, probabilistic, and random forest approaches (columns) compared to PS snow cover frequency (x-axes). Blue areas represent areas with higher point density.

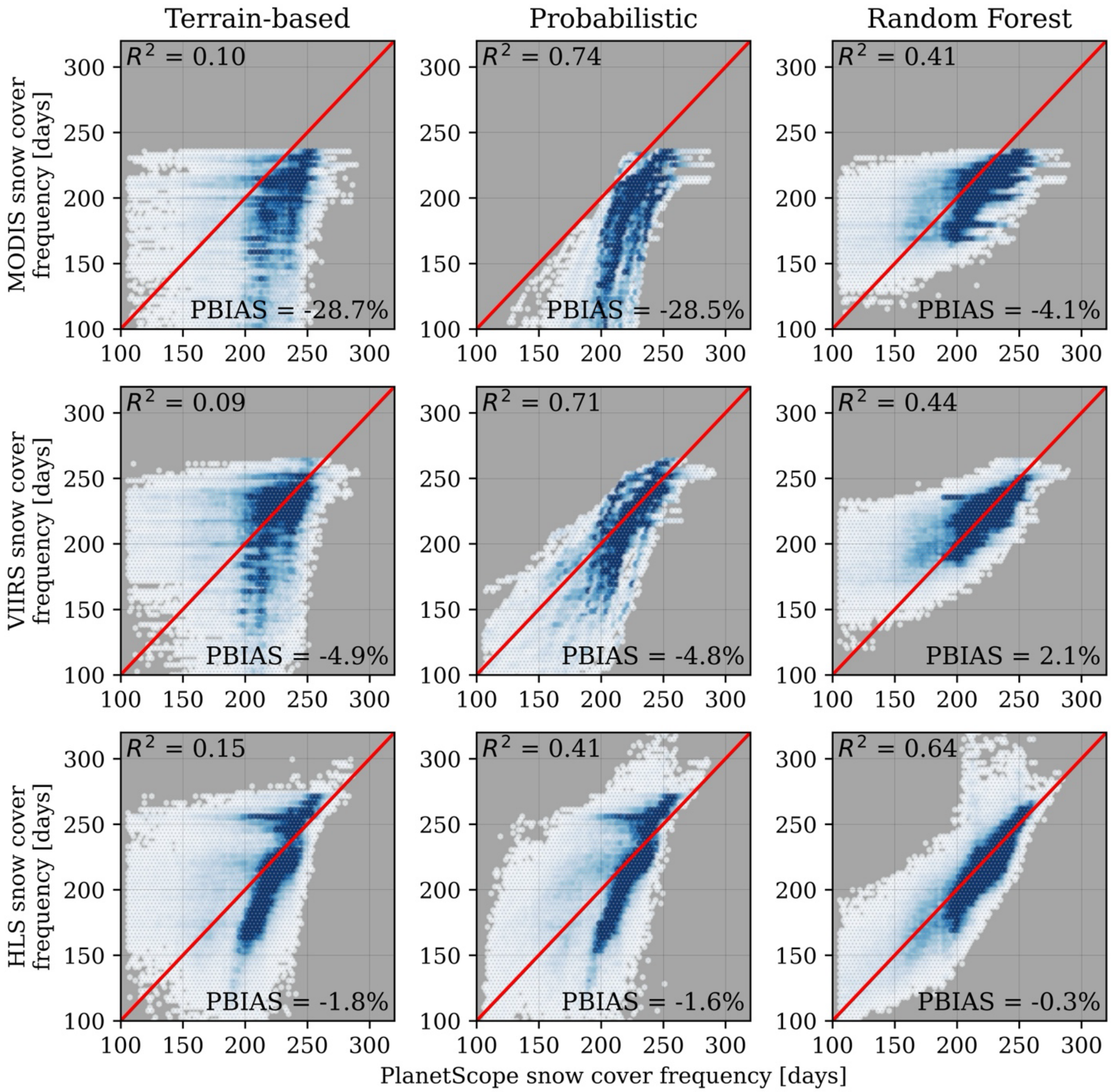

Figure S6. 3 m snow cover frequency estimated in the GIN domain from each sensor (rows) downscaled using the terrain-based, probabilistic, and random forest approaches (columns) compared to PS snow cover frequency (x-axes). Blue areas represent areas with higher point density.

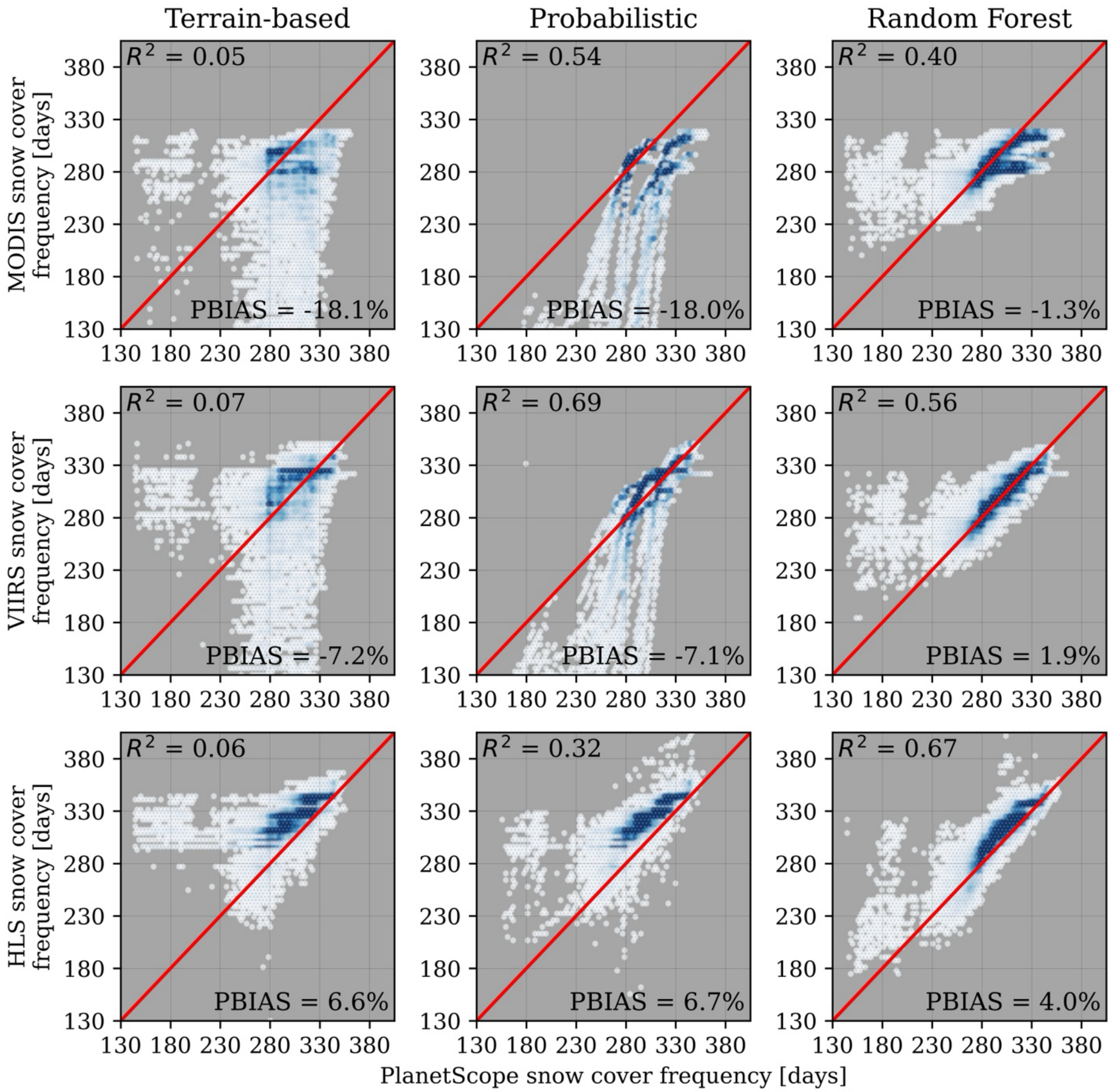

Figure S7. 3 m snow cover frequency estimated in the STR domain from each sensor (rows) downscaled using the terrain-based, probabilistic, and random forest approaches (columns) compared to PS snow cover frequency (x-axes). Blue areas represent areas with higher point density.

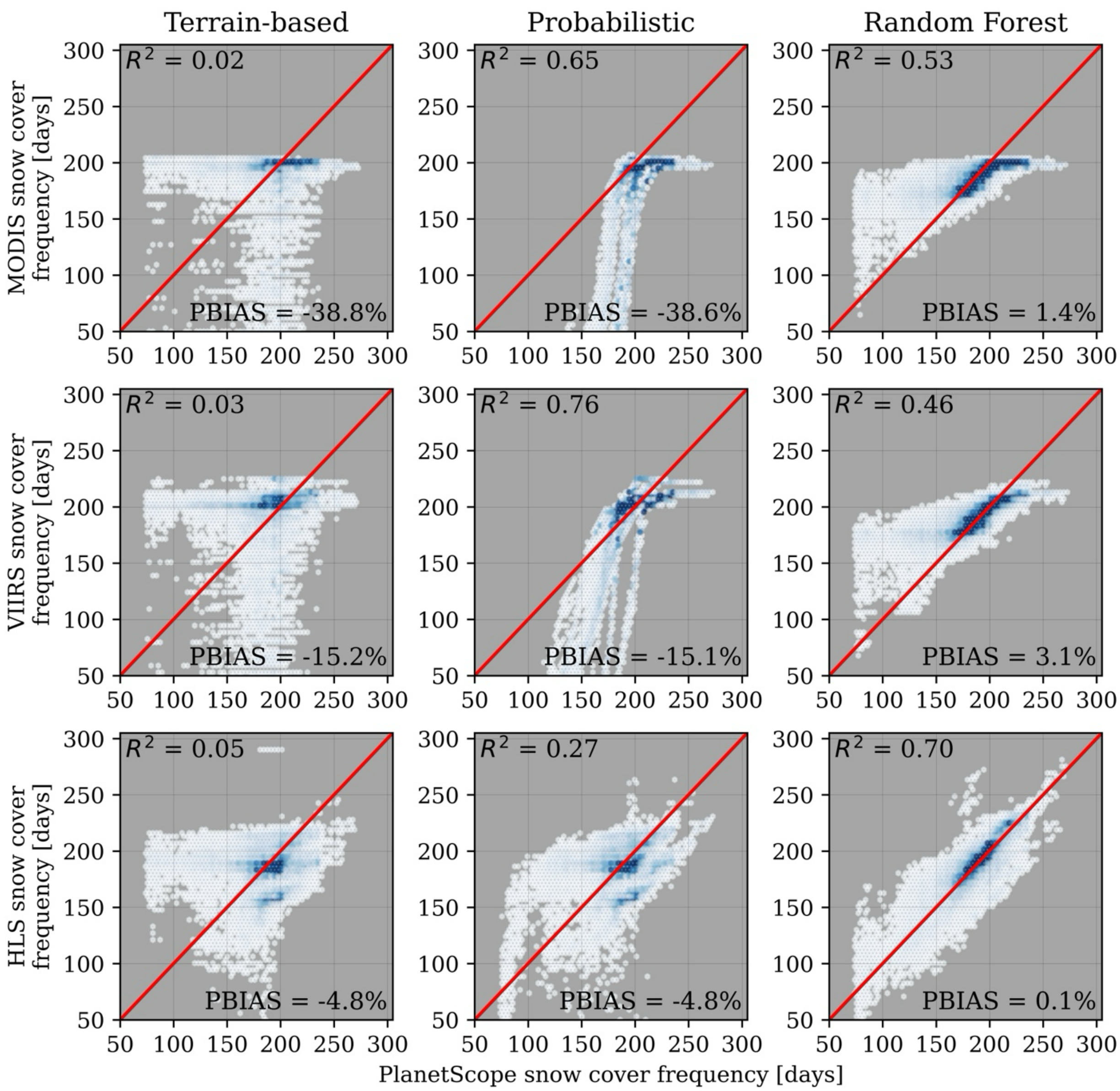

Figure S8. 3 m snow cover frequency estimated in the 551 domain from each sensor (rows) downscaled using the terrain-based, probabilistic, and random forest approaches (columns) compared to PS snow cover frequency (x-axes). Blue areas represent areas with higher point density.

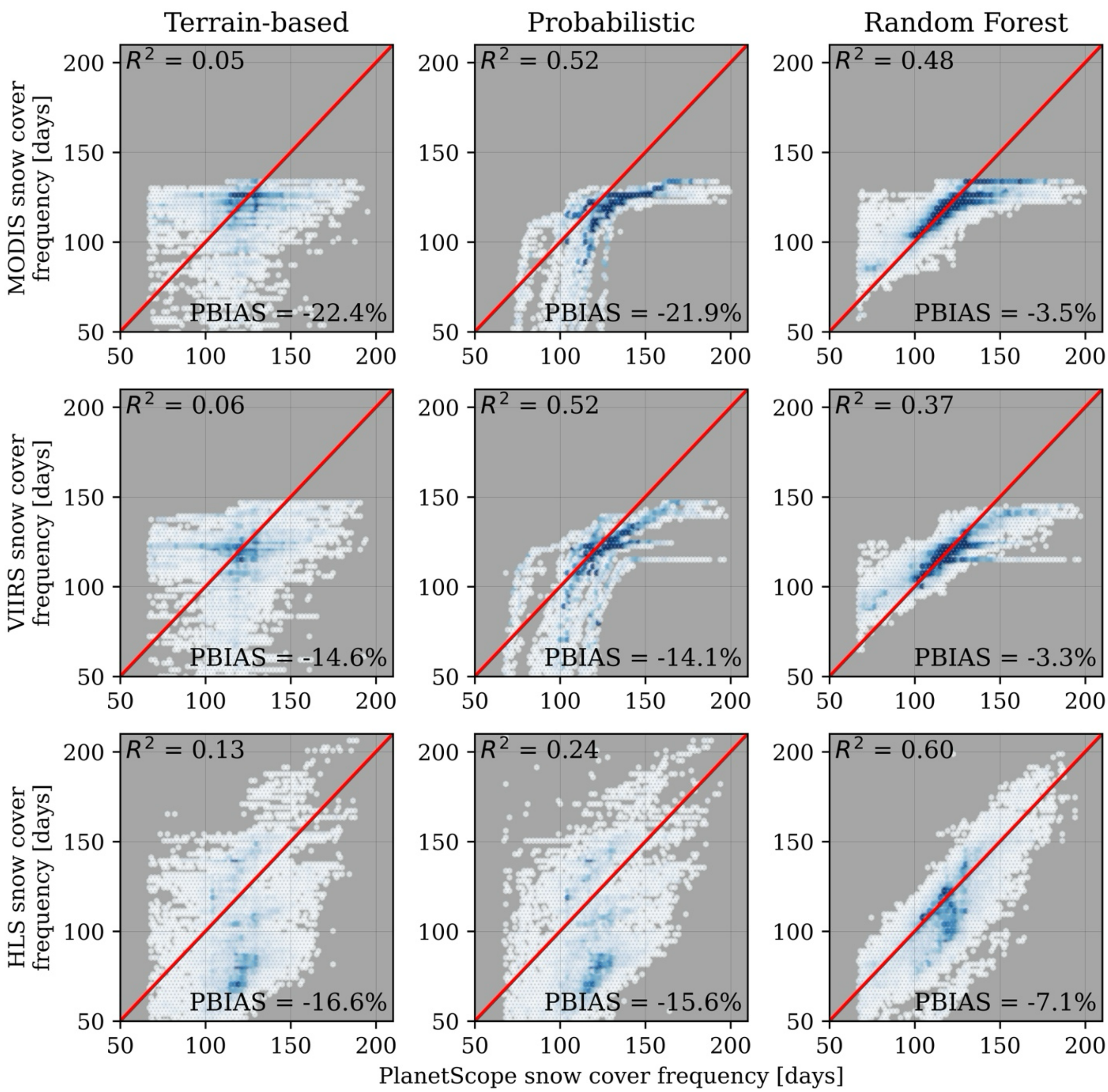

Figure S9. 3 m snow cover frequency estimated in the 869 domain from each sensor (rows) downscaled using the terrain-based, probabilistic, and random forest approaches (columns) compared to PS snow cover frequency (x-axes). Blue areas represent areas with higher point density.

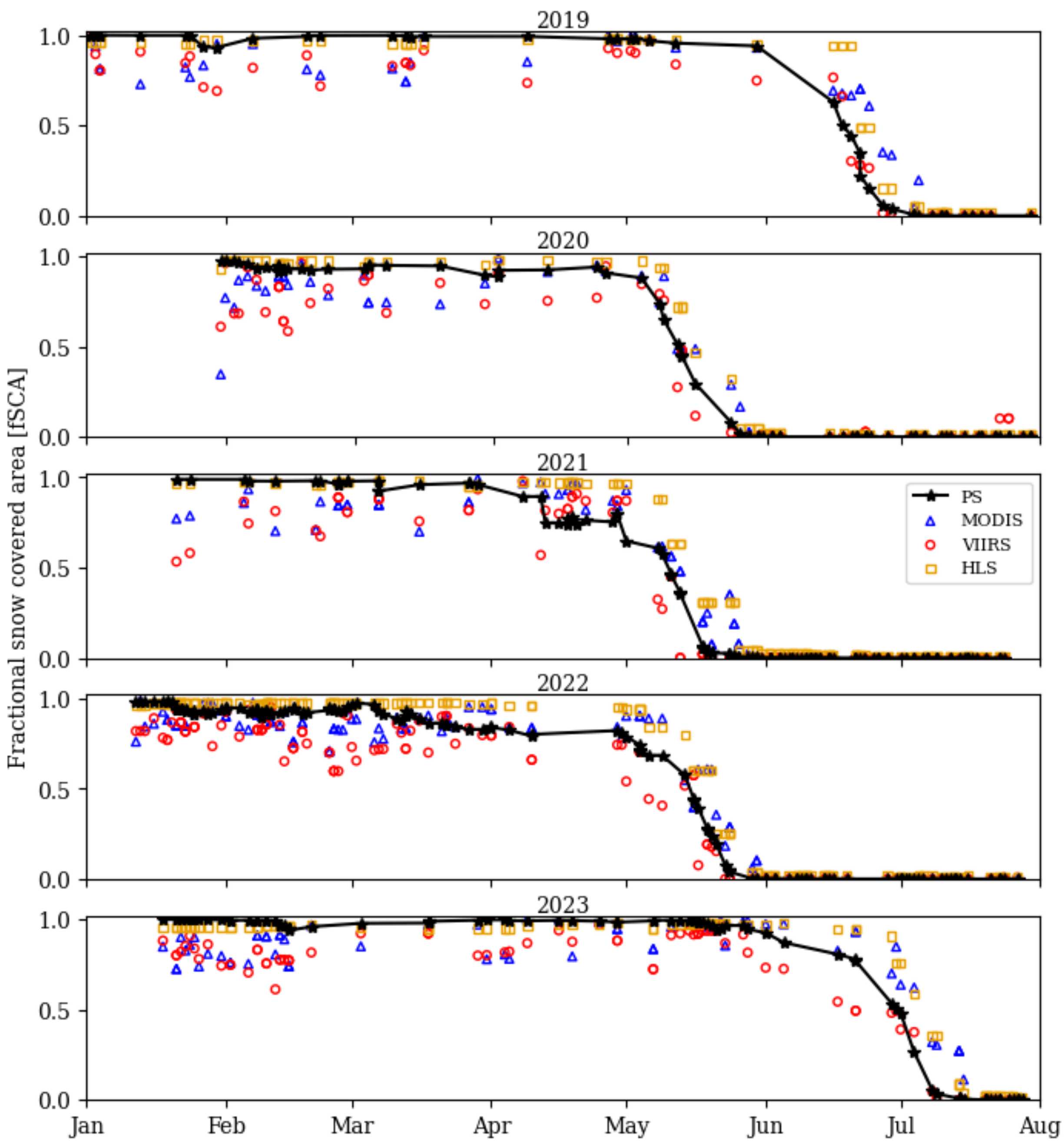

Figure S10. Domain-scale fSCA in DAN for each sensor, relative to PS snow cover estimates.

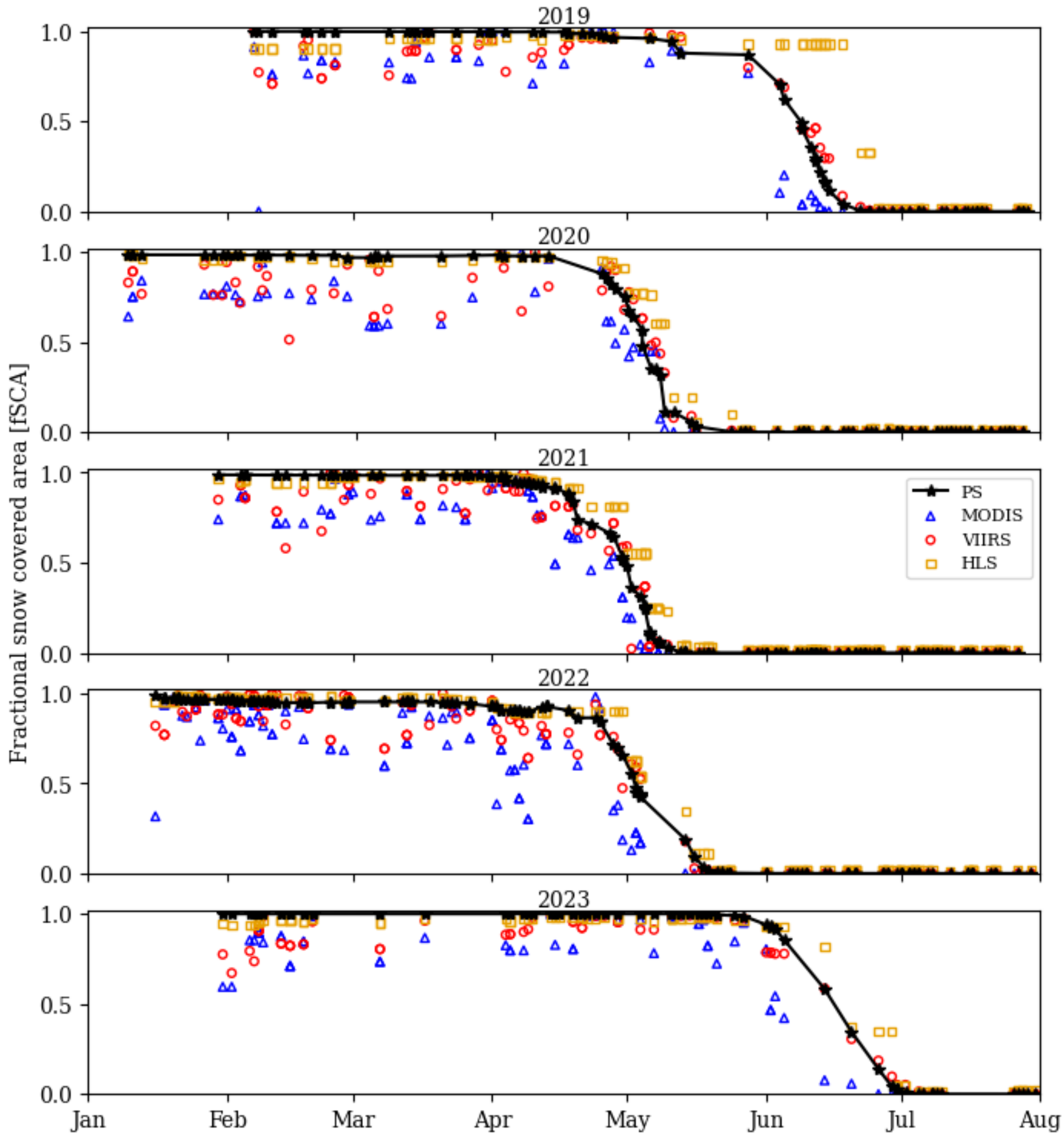

Figure S11. Domain-scale fSCA in STR for each sensor, relative to PS snow cover estimates.

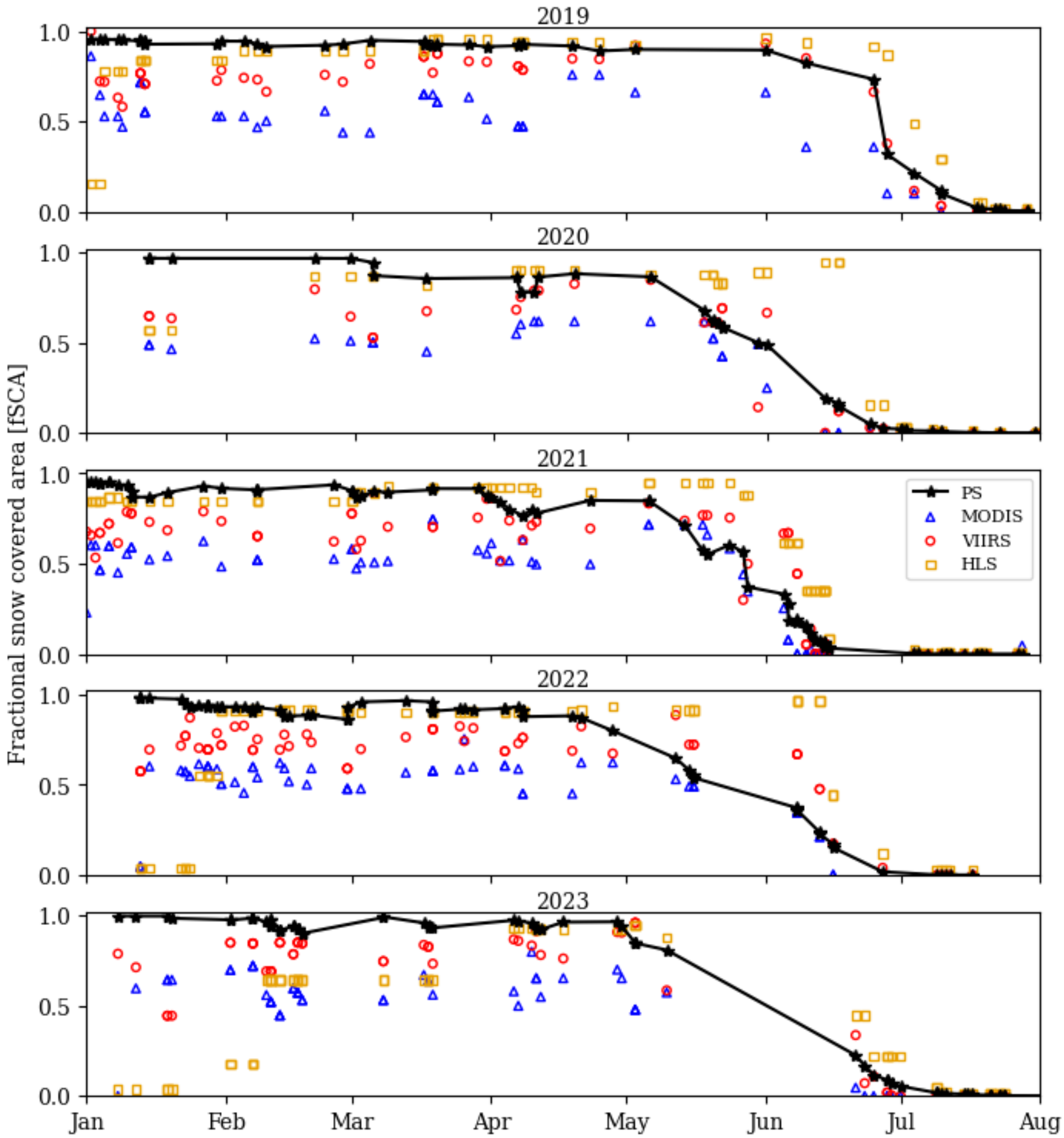

Figure S12. Domain-scale fSCA in 551 for each sensor, relative to PS snow cover estimates.

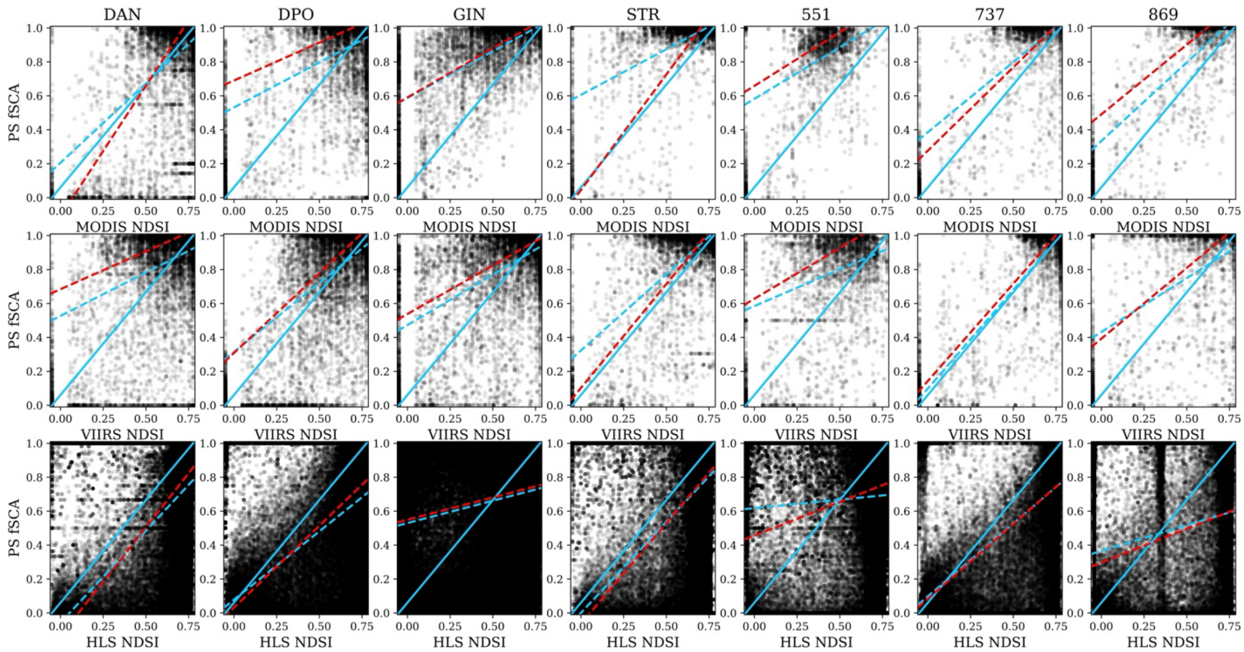

Figure S13. Relationship between NDSI from each sensor (rows, x-axes) and fSCA derived from the underlying 3 m PS pixels for each satellite footprint (y-axes) in each domain (columns). The blue line shows the global conversion (Salomonson and Appel, 2006, 2004) and the dashed blue line shows the best linear fit calculated for each domain and sensor. The red line shows the linear fit calculated including only satellite pixels with less than 5% forest coverage, defined by PS observations.

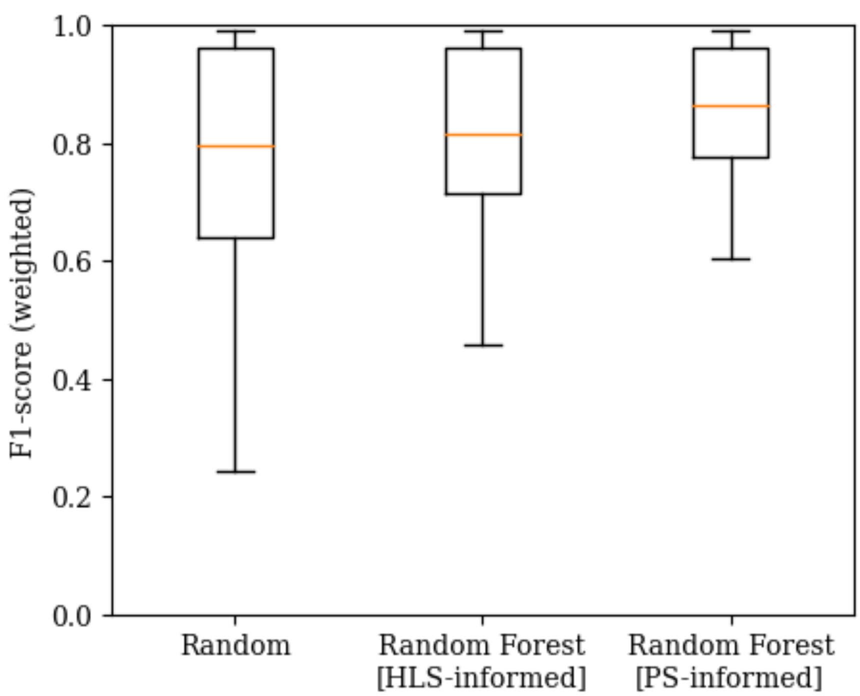

Figure S14. Distribution of weighted F1-scores for snow cover downscaled from MODIS in DPO to 30 m resolutions. In addition to random pixel assignments, snow cover was downscaled using the random forest models trained using snow cover from HLS (middle) and PS coarsened to 30 m resolutions (right). To ensure that the random forest downscaling approach was identical to the approach used to downscale snow cover to 3 m resolutions, snow cover at 30 m resolutions from both HLS and PS were rounded to binary snow presence and absence.

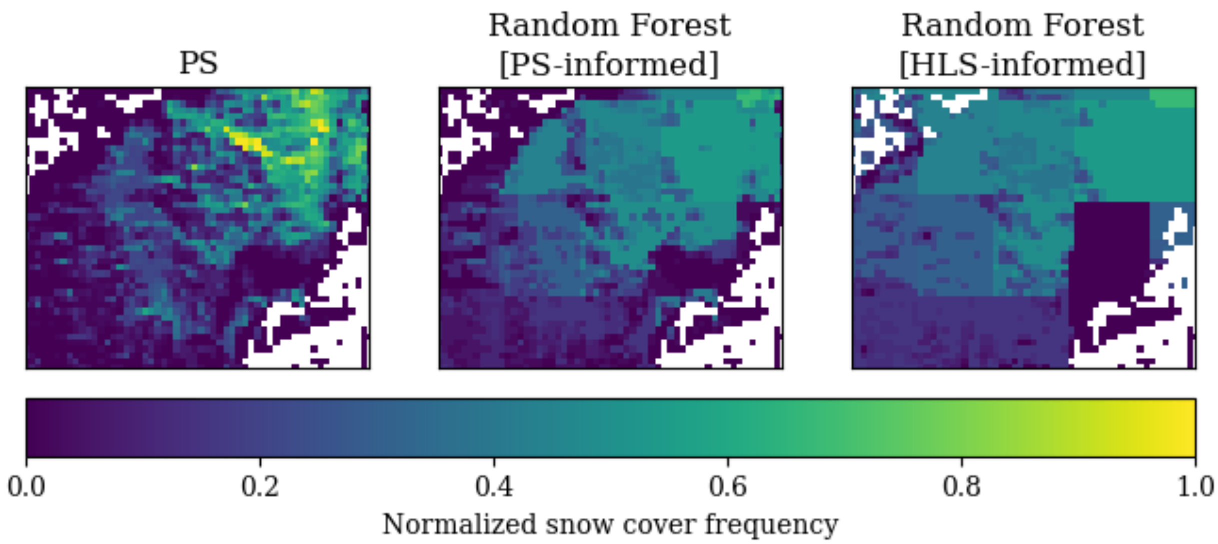

Figure S15. Normalized snow cover frequency in DPO for the 30 m HLS (right) and PS-informed (middle) snow cover downscalings discussed in Figure S14. The additional detail shown by the rightmost subplot presents the frequency of snow cover from PS snow cover maps coarsened to 30m resolutions, but not rounded to binary snow cover.

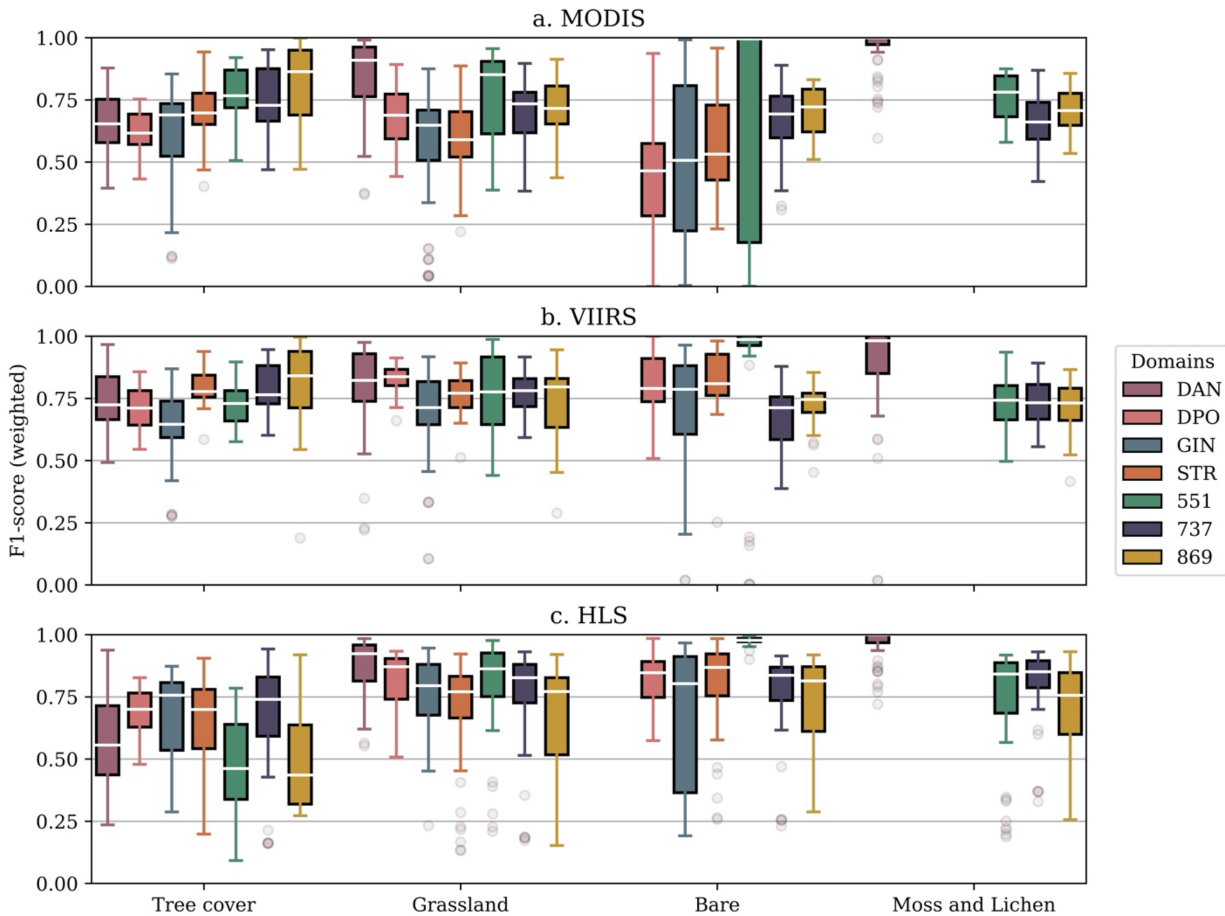

Figure S16. Weighted F1-scores from transitional snow cover days (e.g., Figure 5b) discretized by sensor (subplots), ESA WorldCover landcover type (x ticks), and domains (boxplot color). Results are only shown for domains and landcover types overlapping at least 30 PS cells in at least two domains. Results in this figure are for the 3 m snow cover downscaled using the probabilistic approach. While snow cover was not downscaled for pixels underlying the forest canopy, the "Tree cover" class here represented 3 m pixels that were close enough to the forest canopy to be classified as tree cover from the 10 m ESA WorldCover product.

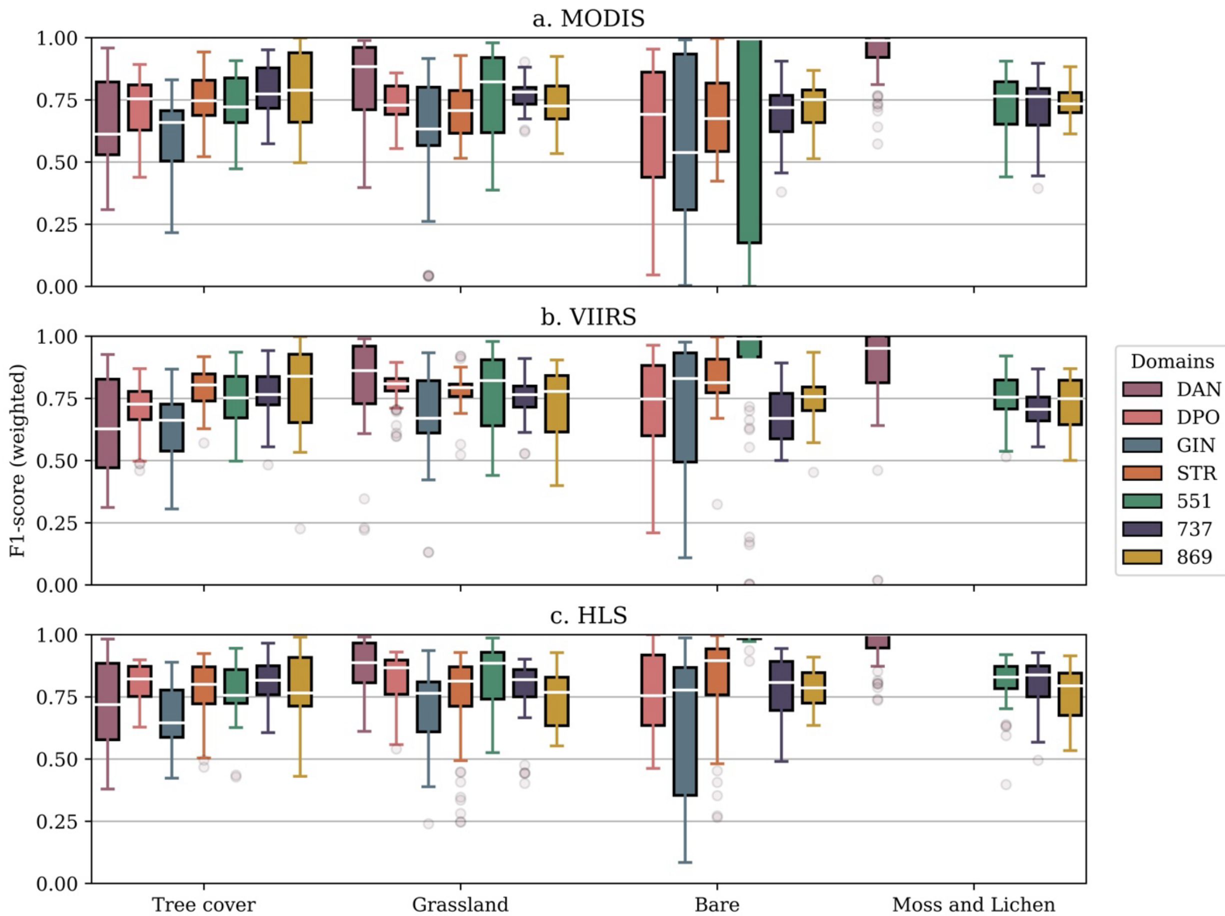

Figure S17. Same plot as Figure S16, but presenting the weighted F1 score for the 3 m snow cover downscaled using the random forest approach.

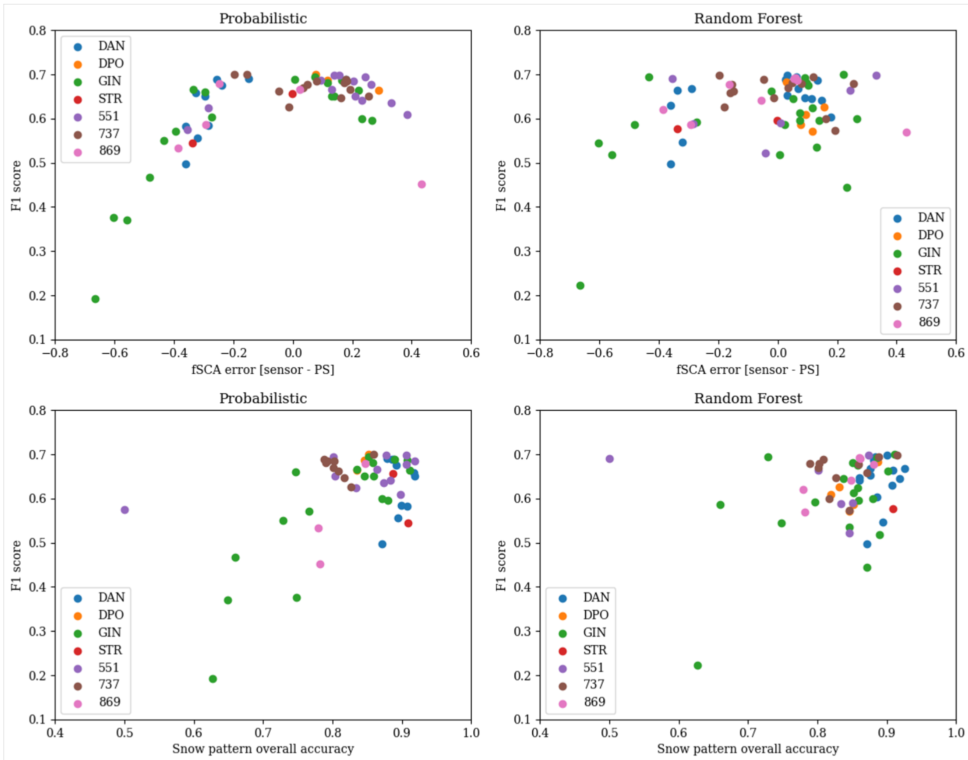

Figure S18. Lower 25th percentile F1-scores plotted relative to the fSCA bias between VIIRS and PS (top plots) and the overall accuracy (fraction of matching snow-present and snow absent pixels) between the PS binary snow cover on each date and average snow cover pattern from the dates with the closest matching PS fSCA from other years (bottom). Results are presented for the probabilistic (left) and random forest (right) models.

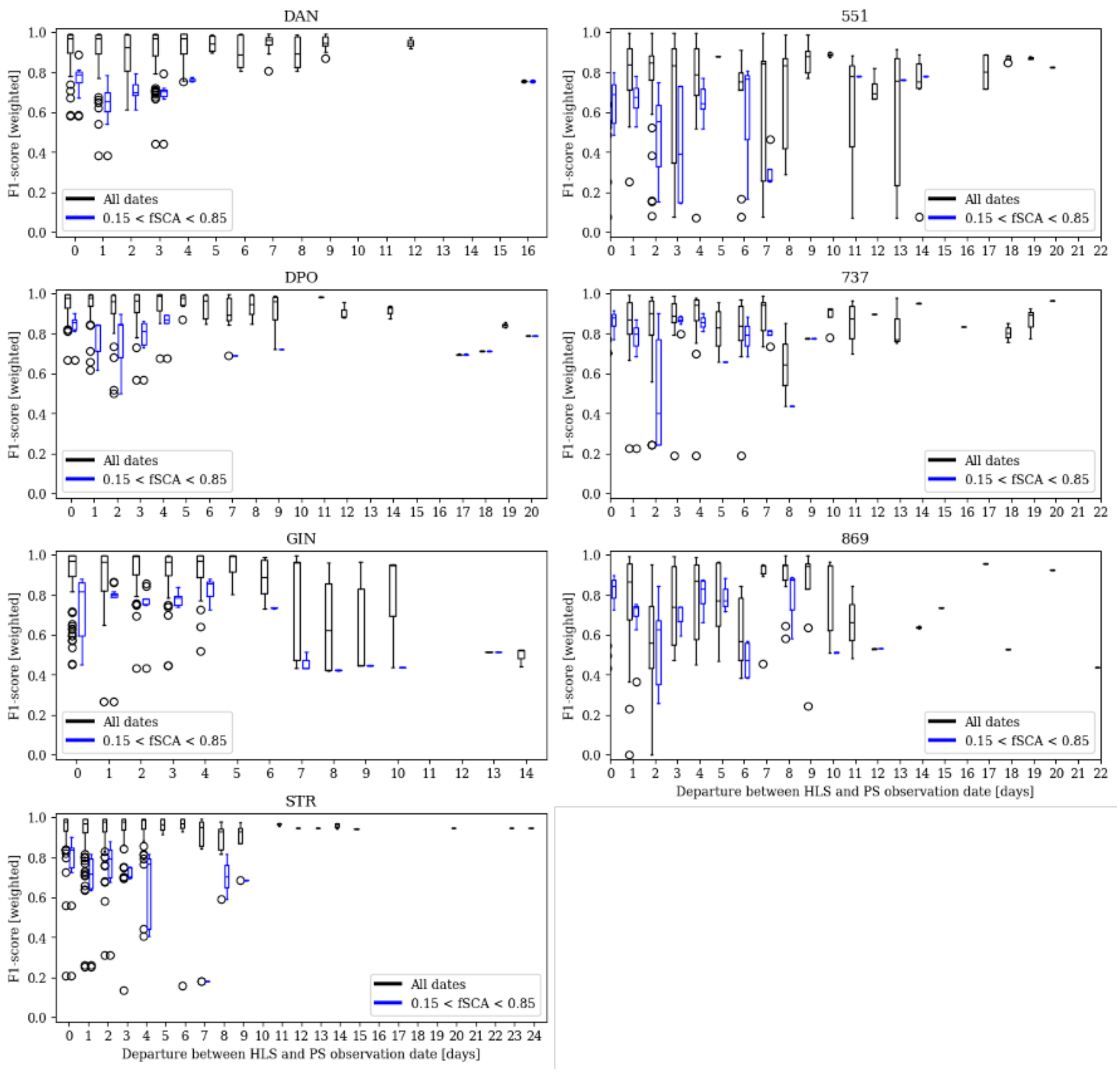

Figure S19. Distribution of F1 scores in all seven domains (subplots) discretized by the departure in time between the PS date and the date that the HLS observation came from as a result of cloud cover (x-axis). Results are for HLS downscaled using the probabilistic approach.

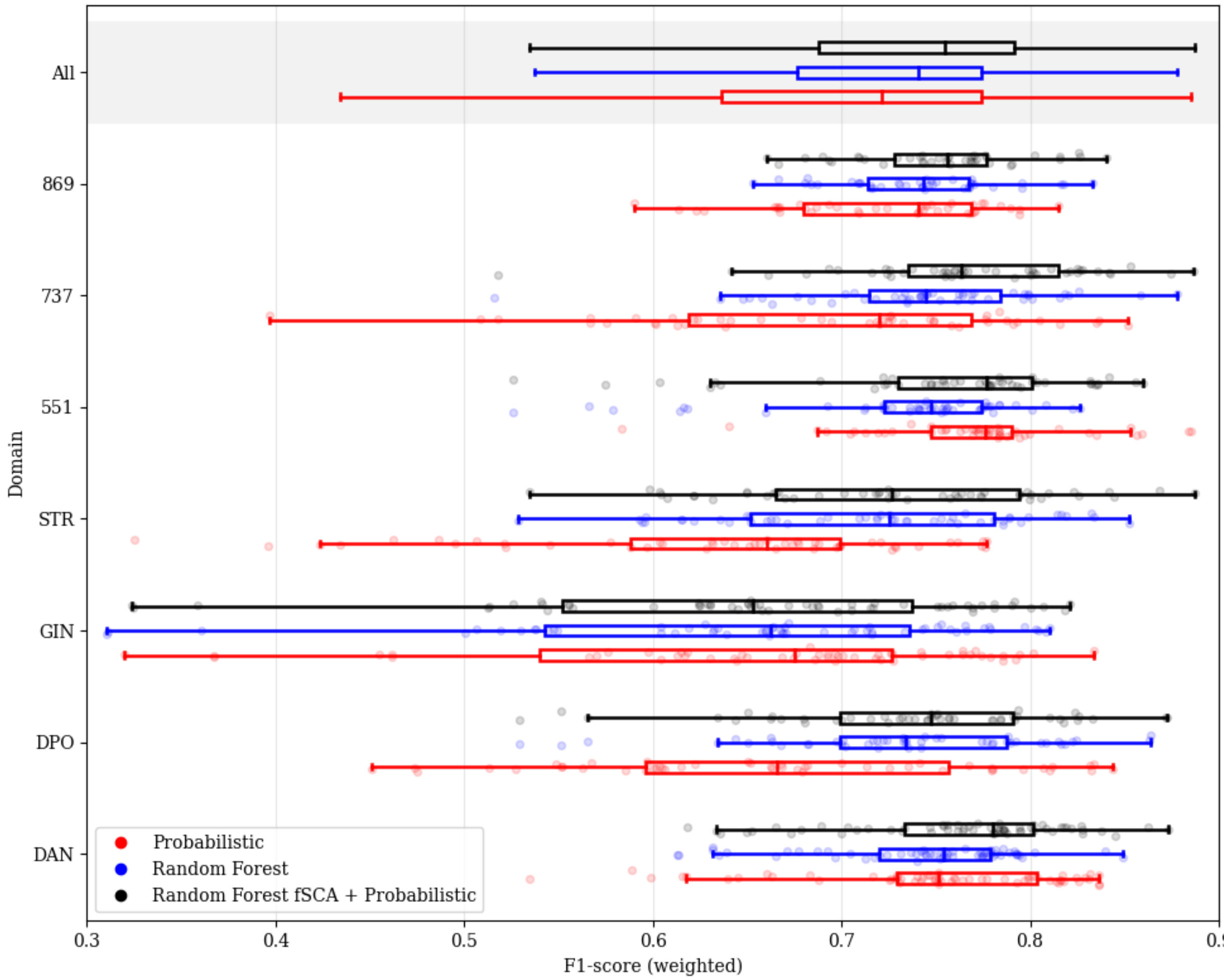

Figure S20. Distribution of F1 scores across the 2019 – 2023 record on dates with partial snow cover (0.15 < fSCA < 0.85) in each domain (y-axis). Results are shown for the probabilistic (red) and RF downscalings (blue), in addition to a downscaling approach providing the bias-corrected fSCA from the RF downscaling to the probabilistic downscaling approach (black).

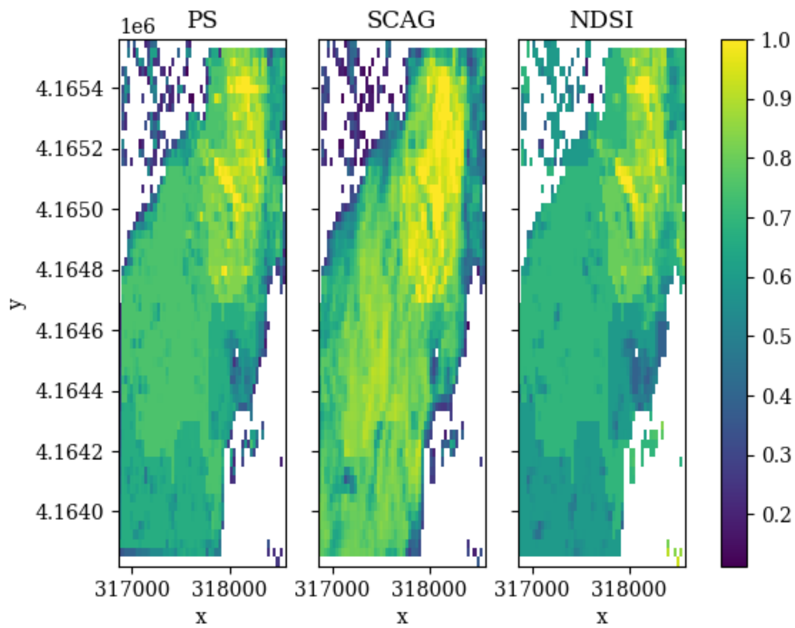

Figure S21. Average snow cover frequency in DPO for Landsat observations accessed from the HLS data between 1 January and 1 July each year between 2019 and 2023 on PS observation dates. For each date, Landsat retrievals were converted to fSCA using the NDSI to fSCA conversion (NDSI; Salomonson and Appel, 2006) and snow covered area and grain size approach (SCAG; Painter et al., 2009). Each scene shows the fSCA summed across all comparison dates (allowing fractional fSCA), and then normalized by dividing by the number of scenes.

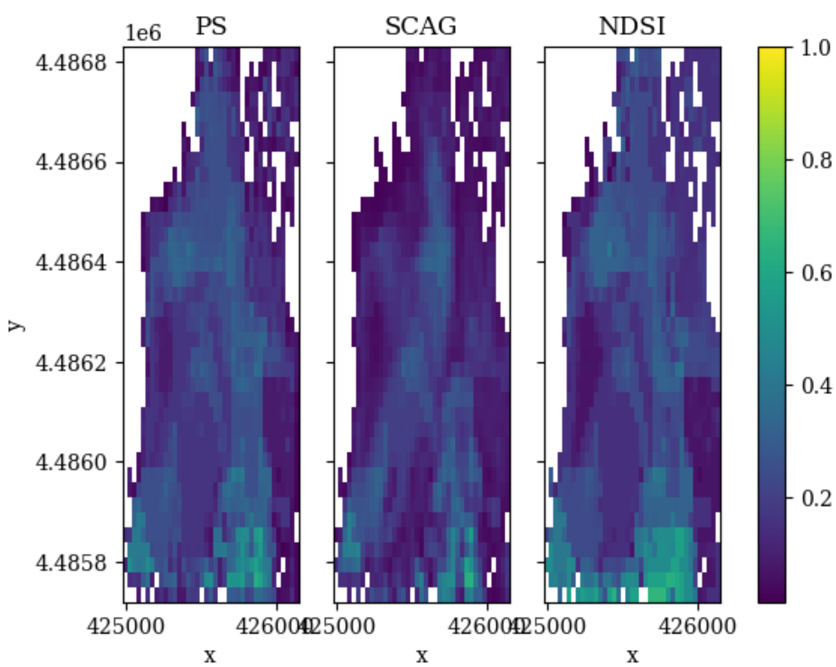

Figure S22. Average snow cover frequency in 551 for Landsat observations accessed from the HLS data between 1 January and 1 July each year between 2019 and 2023 on PS observation dates. For each date, Landsat retrievals were converted to fSCA using the NDSI to fSCA conversion (NDSI; Salomonson and Appel, 2006) and snow covered area and grain size approach (SCAG; Painter et al., 2009). Each scene shows the fSCA summed across all comparison dates (allowing fractional fSCA), and then normalized by dividing by the number of scenes.

Painter, T.H., Rittger, K., McKenzie, C., Slaughter, P., Davis, R.E., Dozier, J., 2009. Retrieval of subpixel snow covered area, grain size, and albedo from MODIS. Remote Sens. Environ. 113, 868–879. https://doi.org/10.1016/j.rse.2009.01.001

Salomonson, V.V., Appel, I., 2006. Development of the Aqua MODIS NDSI fractional snow cover algorithm and validation results. IEEE Trans. Geosci. Remote Sens. 44, 1747–1756. https://doi.org/10.1109/TGRS.2006.876029

Salomonson, V.V., Appel, I., 2004. Estimating fractional snow cover from MODIS using the normalized difference snow index. Remote Sens. Environ. 89, 351–360. https://doi.org/10.1016/j.rse.2003.10.016